Supporting Information:

Structurally versatile phosphine and amine donors constructed from N-heterocyclic olefin units

Nathan R. Paisley, Melanie W. Lui, Robert McDonald, Michael J. Ferguson, Eric Rivard*

Contents

Figure S1. ^{1}H NMR spectrum of (IPr=CH)P^{i}Pr$_2$ (**2**) in C_6D_6.

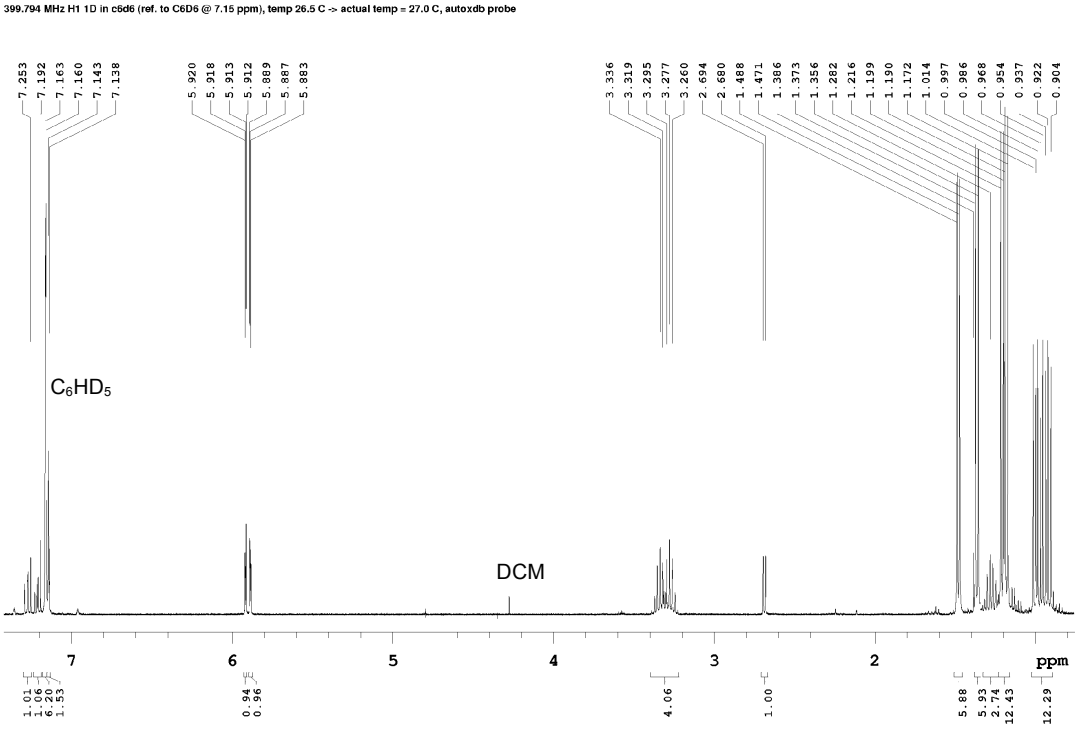

Figure S2. $^{13}C\{^{1}H\}$ DEPTQ NMR spectrum of (IPr=CH)P^{i}Pr$_2$ (**2**) in C_6D_6.

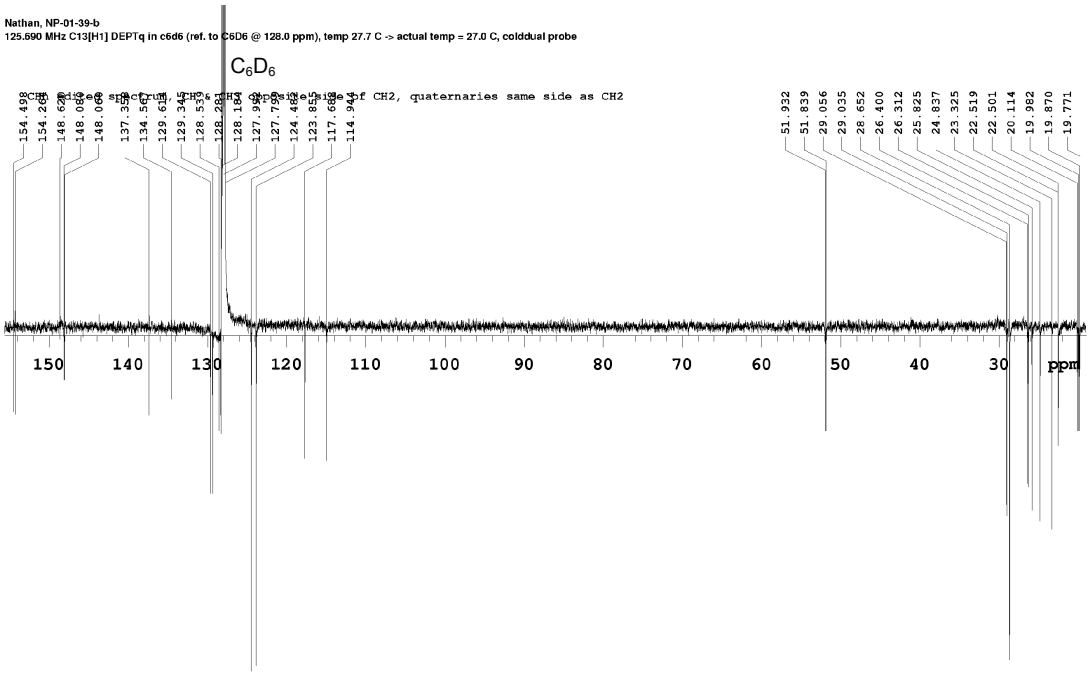

Figure S3. $^{31}P\{^{1}H\}$ NMR spectrum of (IPr=CH)P^{i}Pr$_2$ (**2**) in C_6D_6.

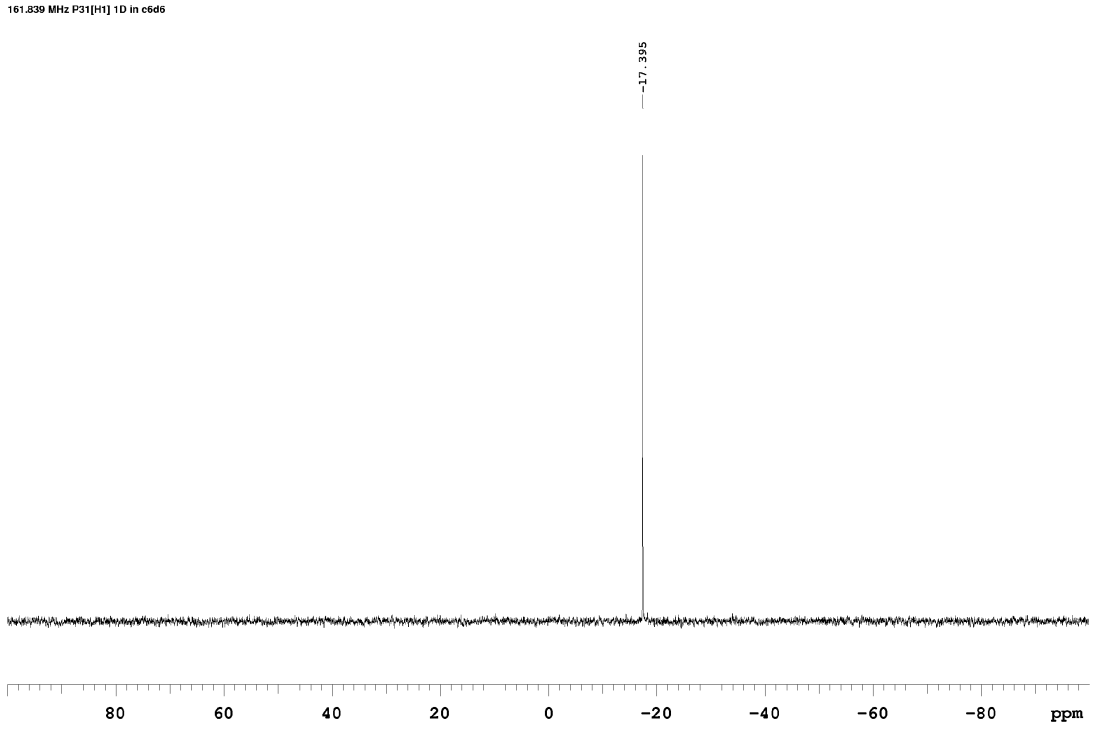

Figure S4. ^{1}H NMR spectrum of (IPr=CH)PPh_2 (**3**) in C_6D_6.

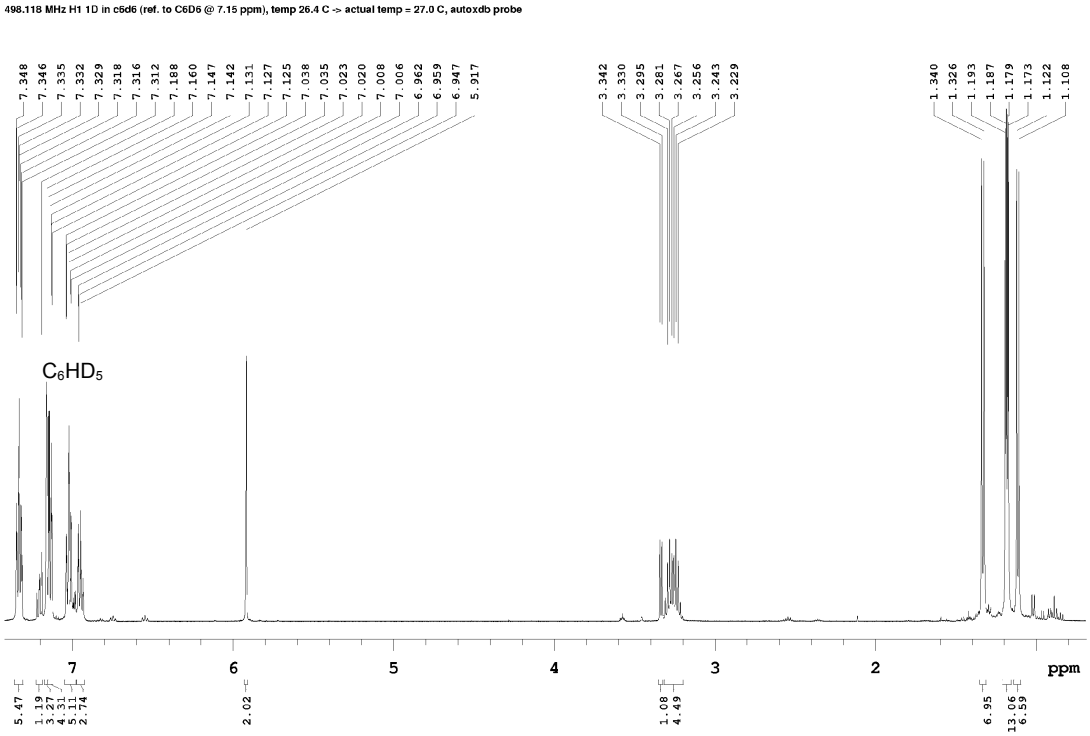

Figure S5. $^{13}C\{^{1}H\}$ DEPTQ NMR spectrum of (IPr=CH)PPh_2 (**3**) in C_6D_6.

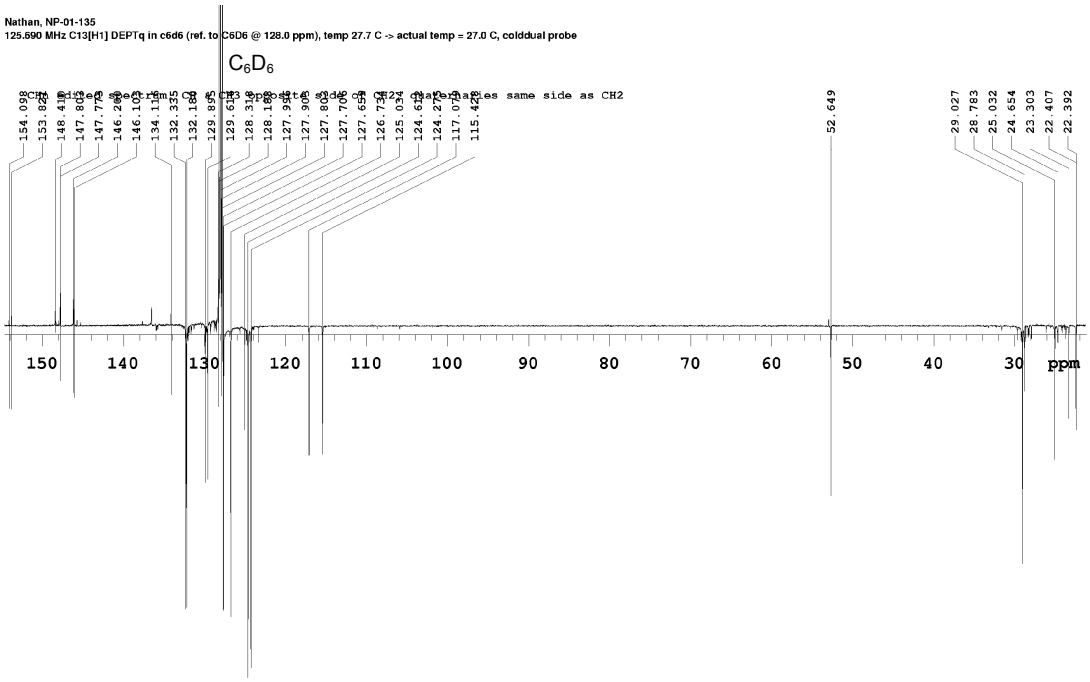

Figure S6. $^{31}P\{^{1}H\}$ NMR spectrum of (IPr=CH)PPh_2 (**3**) in C_6D_6.

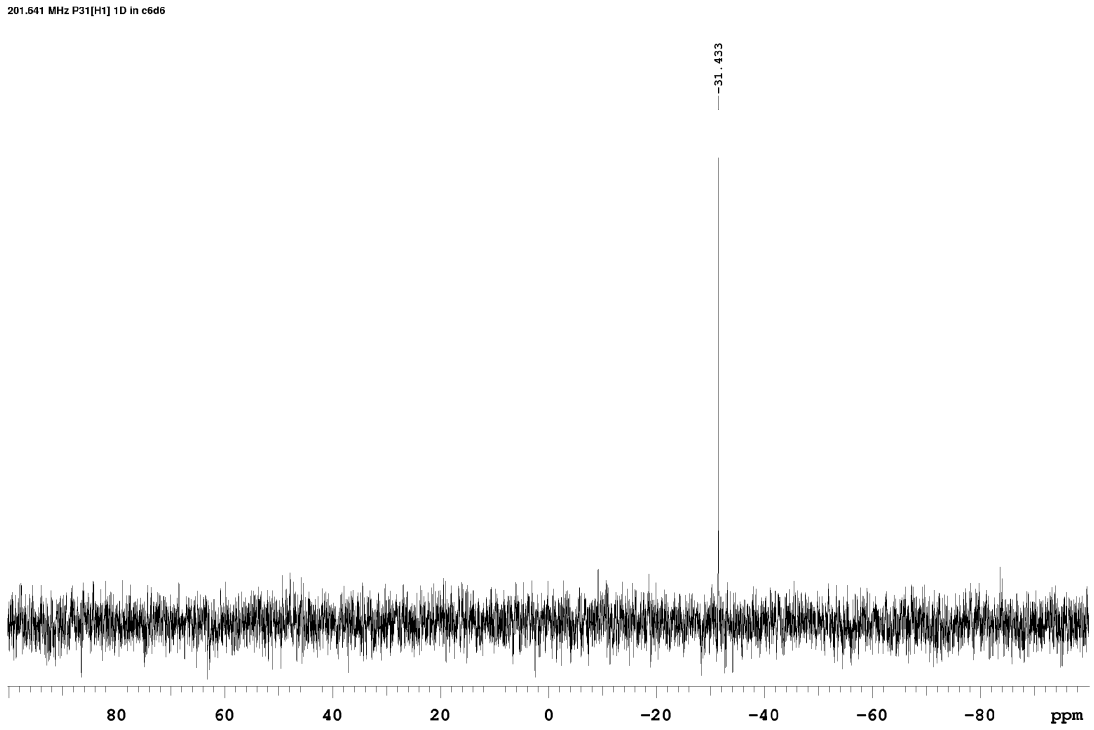

Figure S7. ^{1}H NMR spectrum of (IPr=CH)NMe_2 (**4**) in C_6D_6.

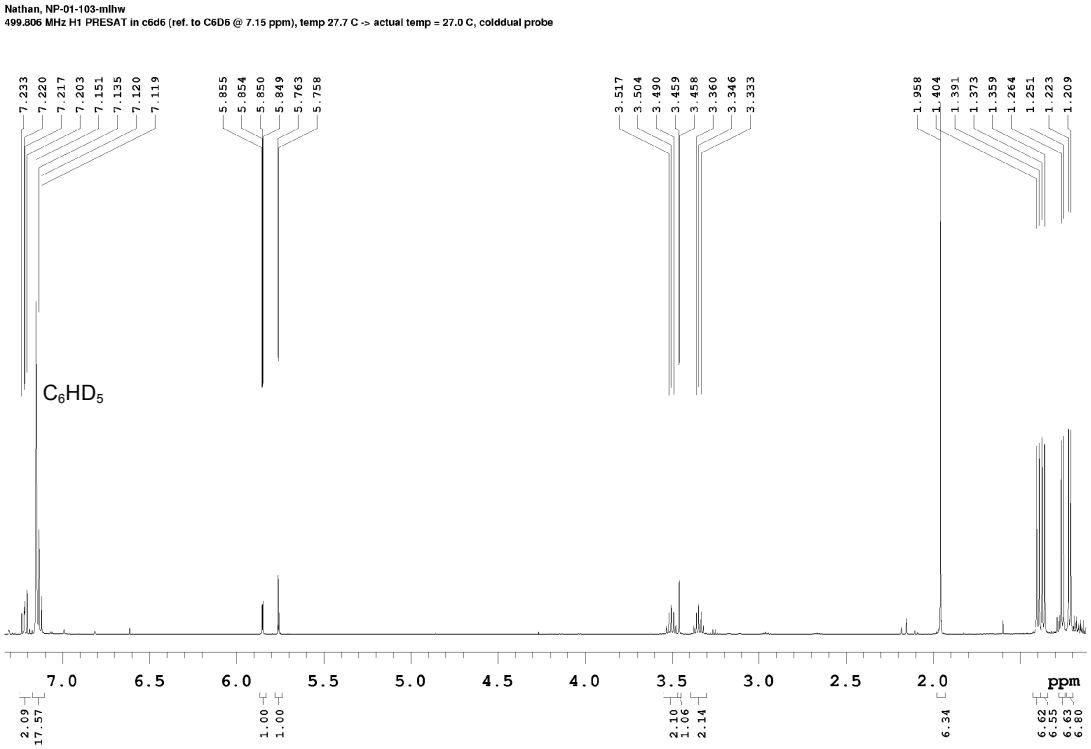

Figure S8. $^{13}C\{^{1}H\}$ DEPTQ NMR spectrum of (IPr=CH)NMe_2 (**4**) in C_6D_6.

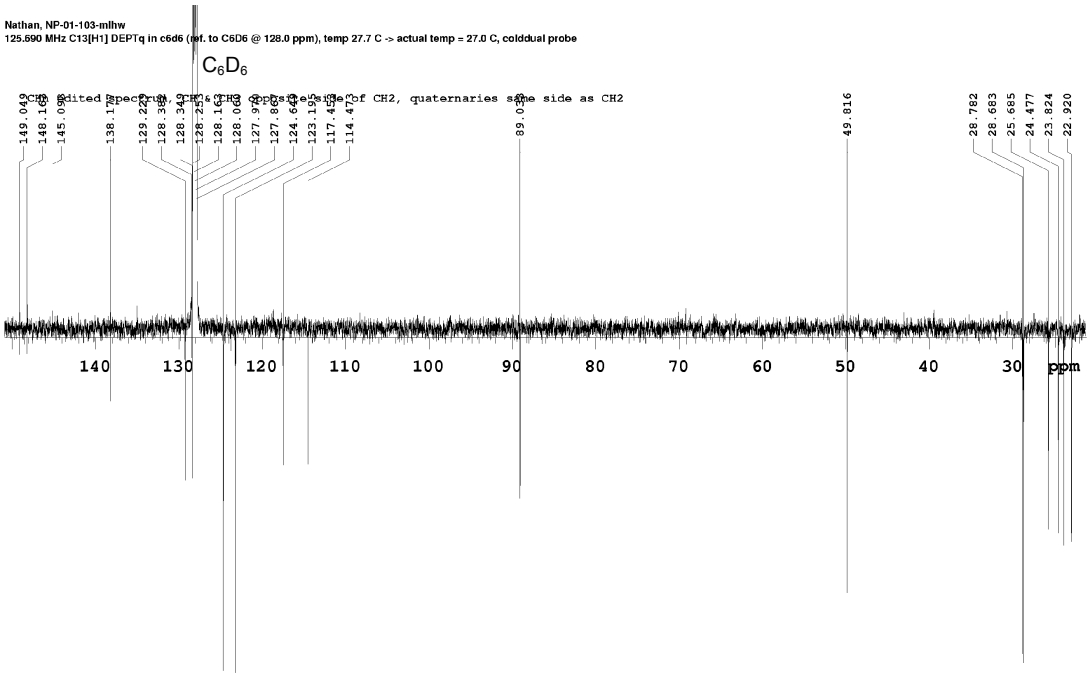

Figure S9. ^{1}H NMR spectrum of (IPr=CH)^{i}Pr$_2$P•BH$_3$ (**5**) in C_6D_6.

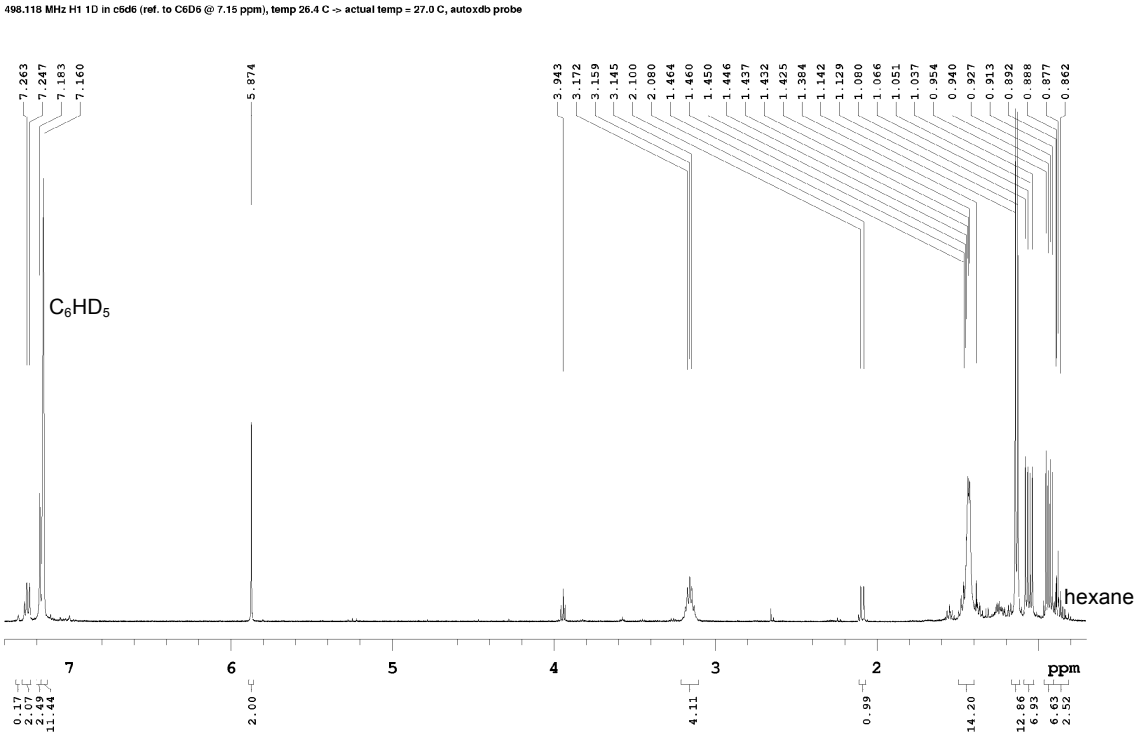

Figure S10. $^{11}B\{^{1}H\}$ NMR spectrum of (IPr=CH)^{i}Pr$_2$P•BH$_3$ (**5**) in C_6D_6.

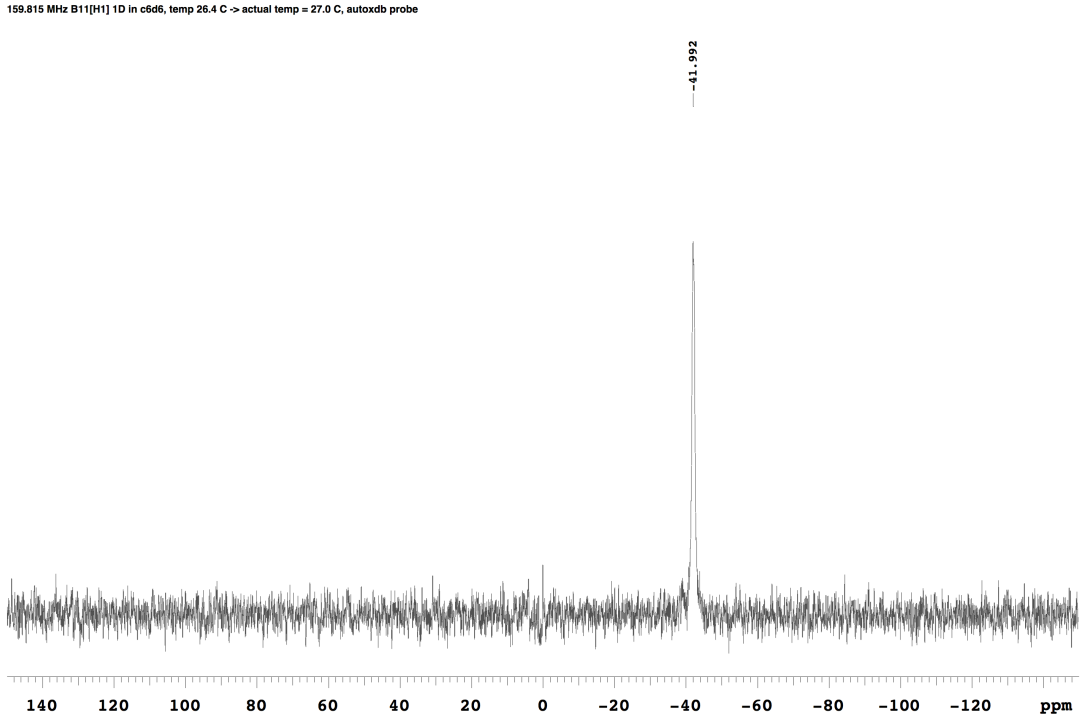

C_6D_6

Figure S11. $^{13}C\{^1H\}$ DEPTQ NMR spectrum of (IPr=CH)^{i}Pr$_2$P•BH$_3$ (**5**) in C_6D_6.

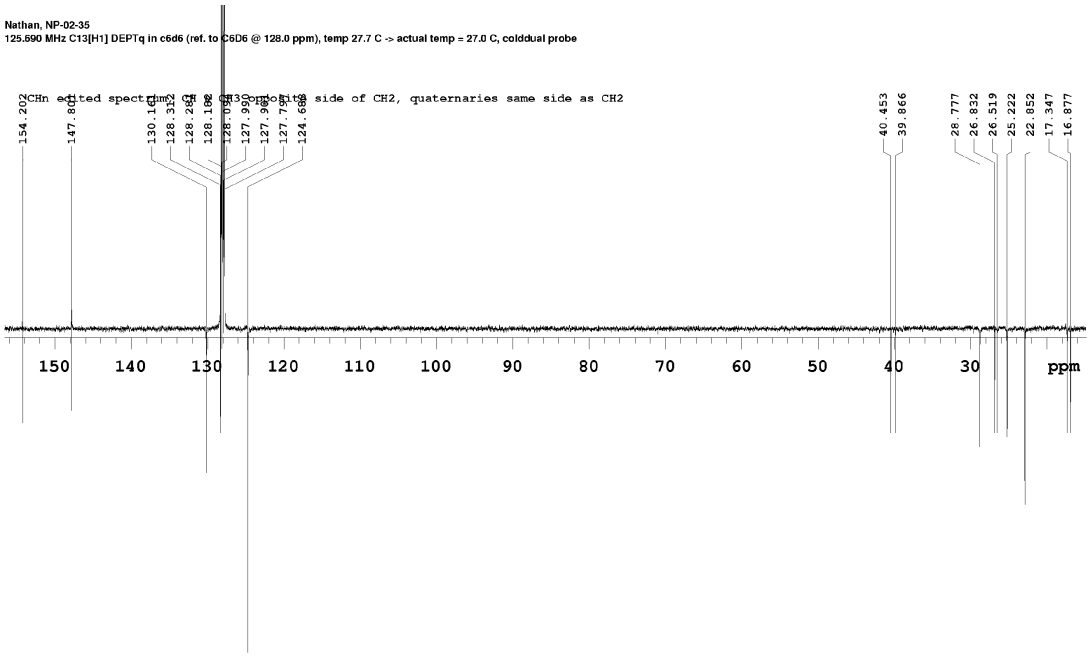

Figure S12. $^{31}P\{^{1}H\}$ NMR spectrum of (IPr=CH)^{i}Pr$_2$P•BH$_3$ (**5**) in C_6D_6.

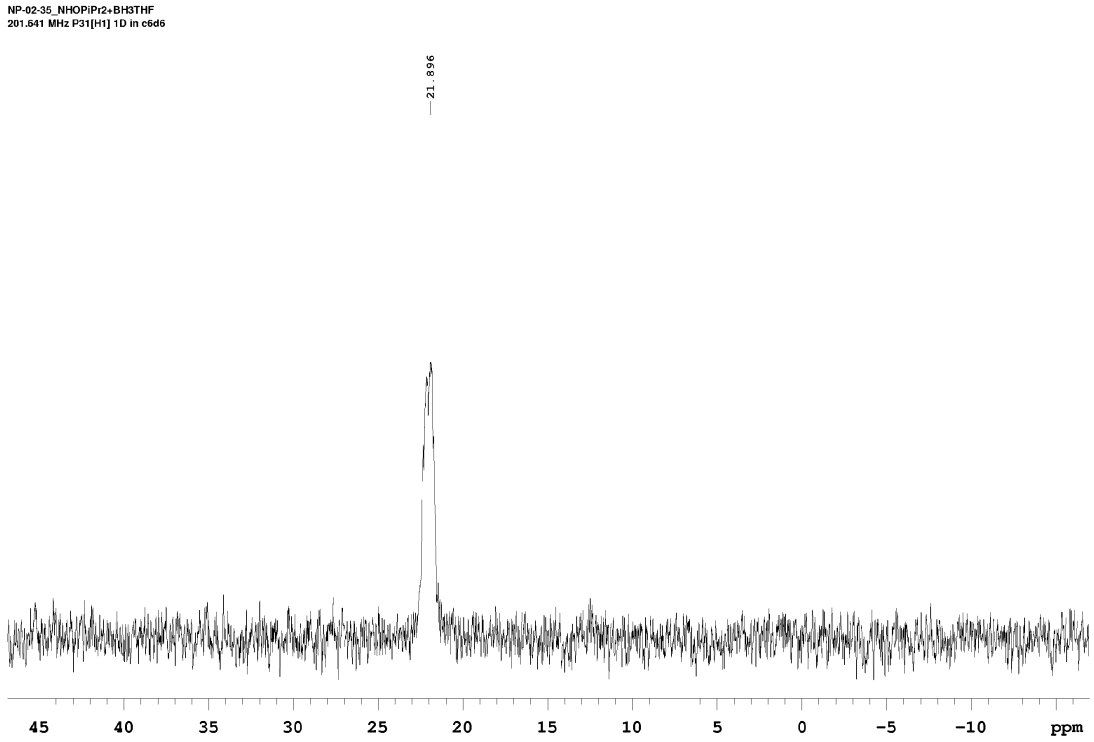

Figure S13. ^{1}H NMR spectrum of (IPr=CH)Ph_2P•BH_3 (**6**) in C_6D_6.

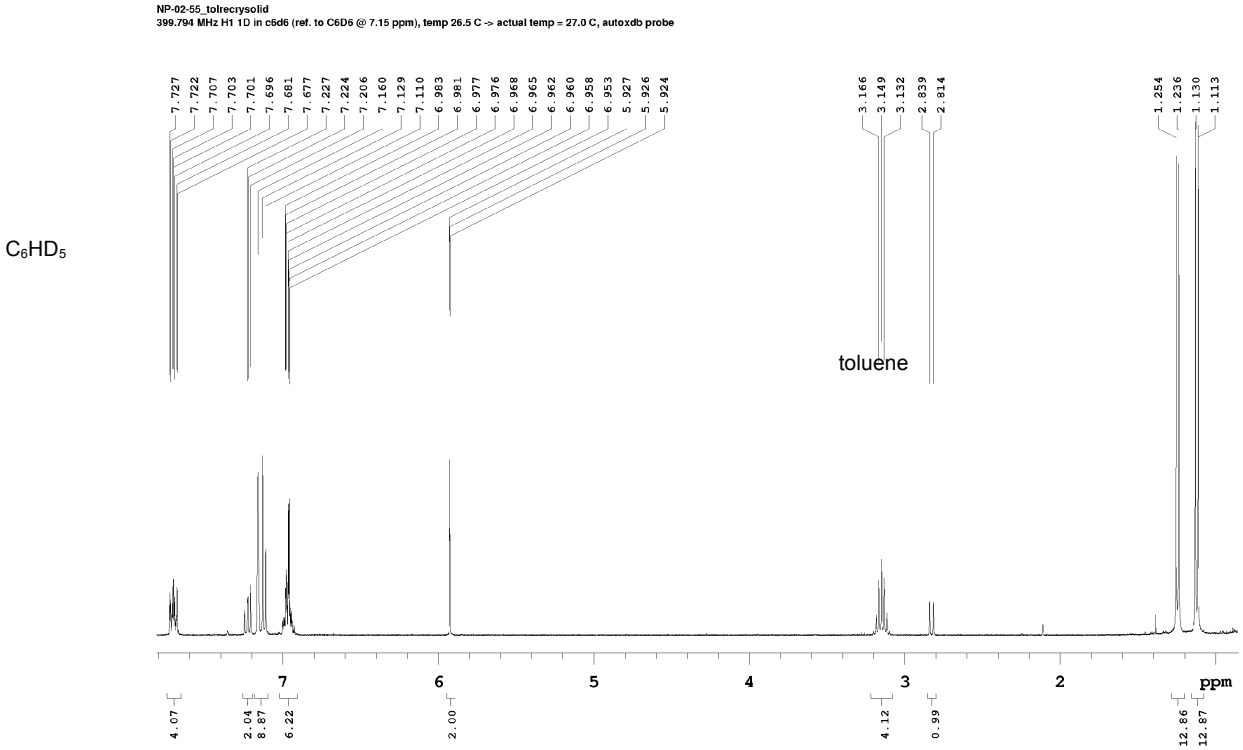

Figure S14. $^{11}B\{^{1}H\}$ NMR spectrum of (IPr=CH)Ph_2P•BH_3 (**6**) in C_6D_6.

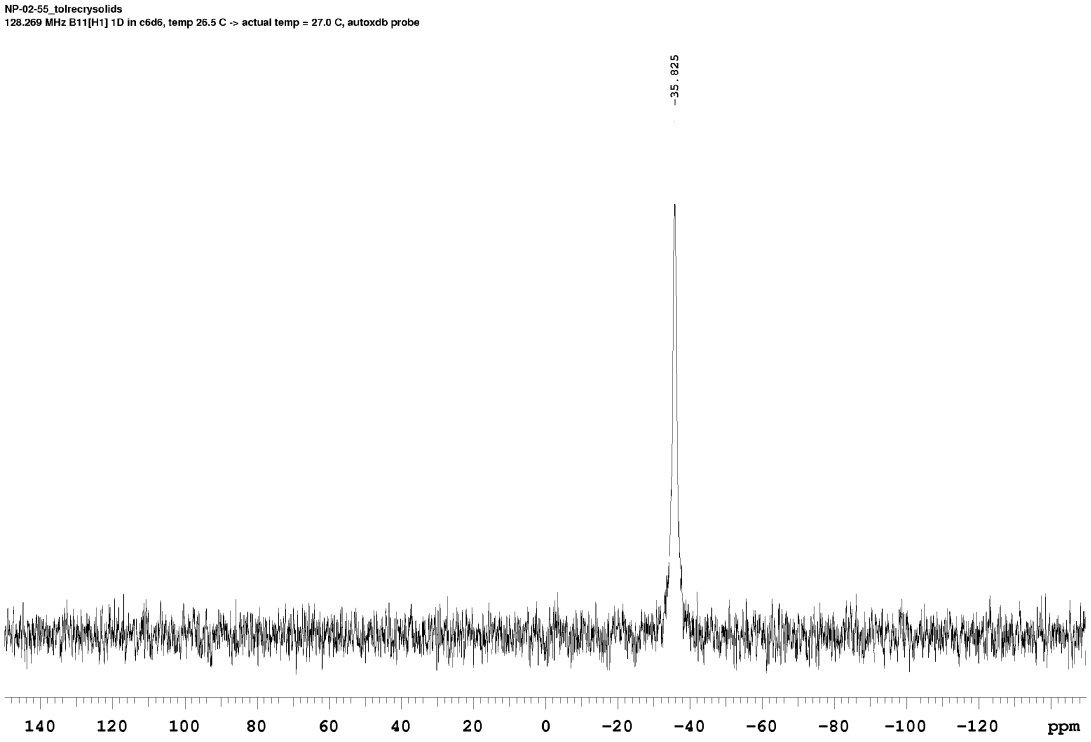

C_6D_6

Figure S15. $^{13}C\{^1H\}$ DEPTQ NMR spectrum of (IPr=CH)Ph_2P•BH_3 (**6**) in C_6D_6.

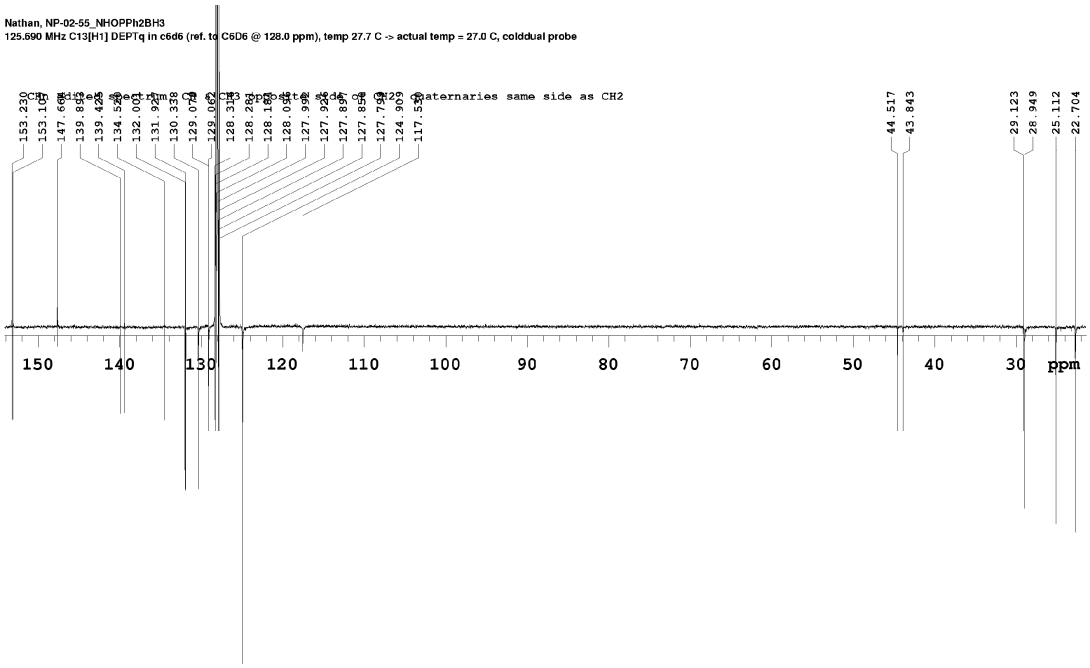

Figure S16. $^{31}P\{^{1}H\}$ NMR spectrum of (IPr=CH)Ph_2P•BH_3 (**6**) in C_6D_6.

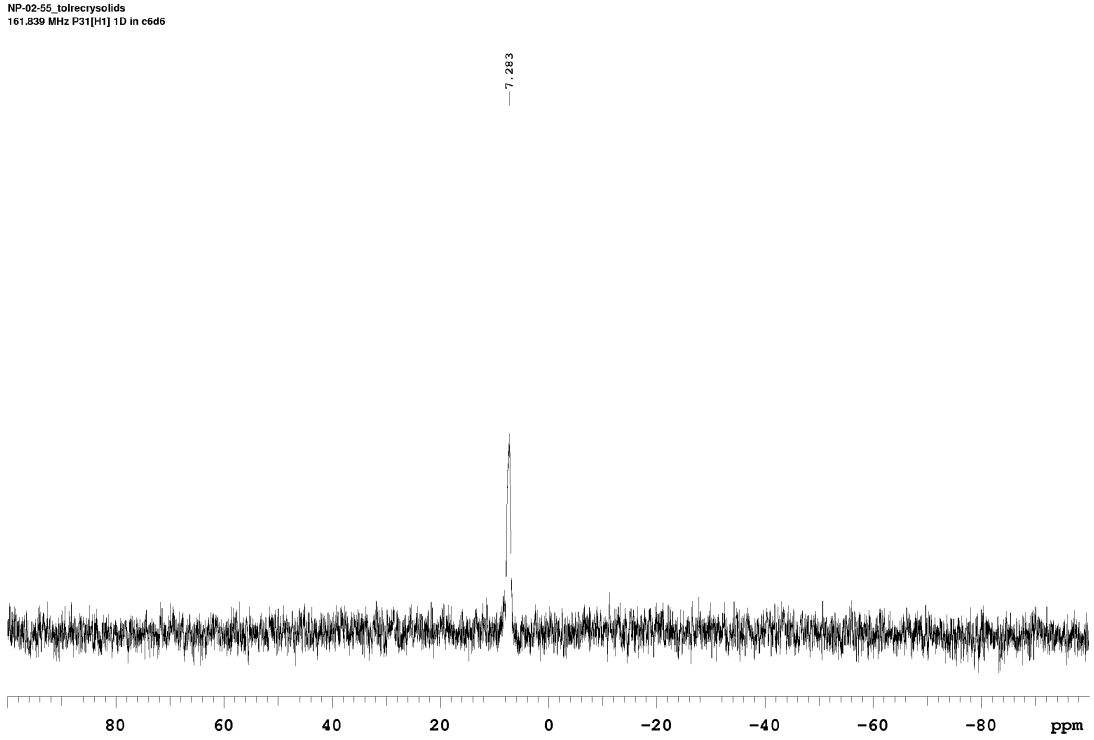

Figure S17. ^{1}H NMR spectrum of (IPr=CH)^{i}Pr$_2$P•PdCl(cinnamyl) (**7**) in C_6D_6.

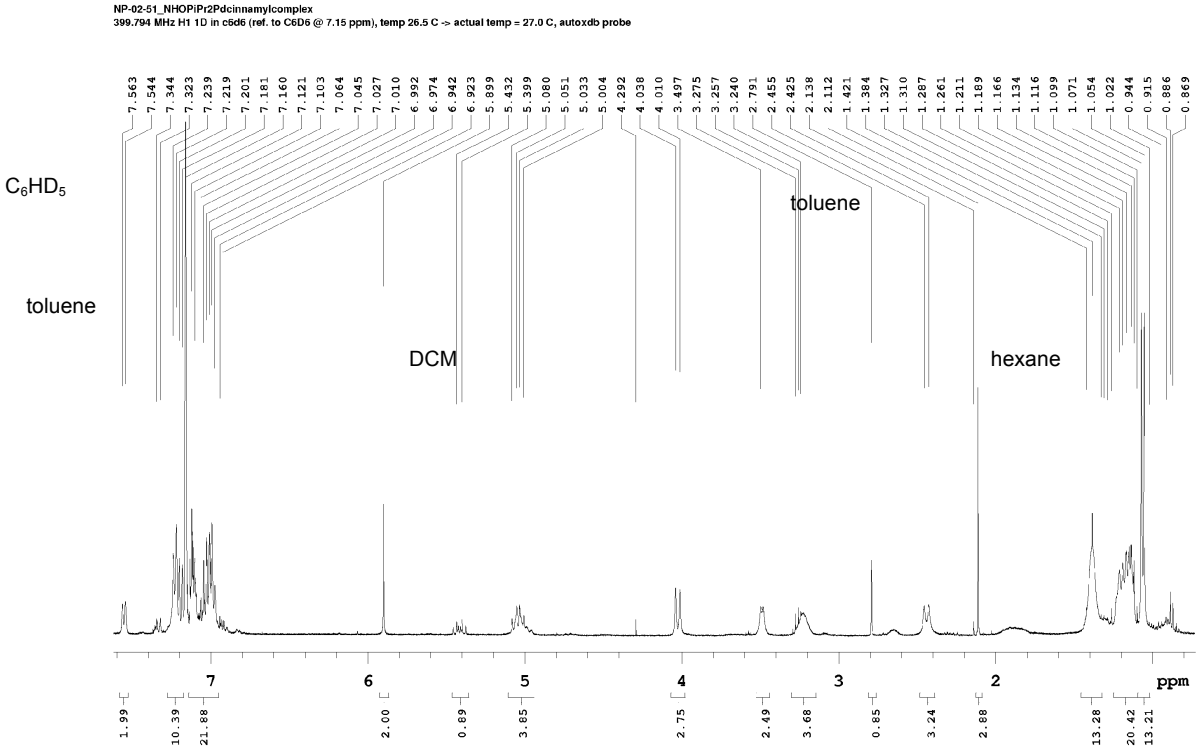

Figure S18. $^{31}P\{^{1}H\}$ NMR spectrum of (IPr=CH)^{i}Pr$_2$P•PdCl(cinnamyl) (**7**) in C_6D_6.

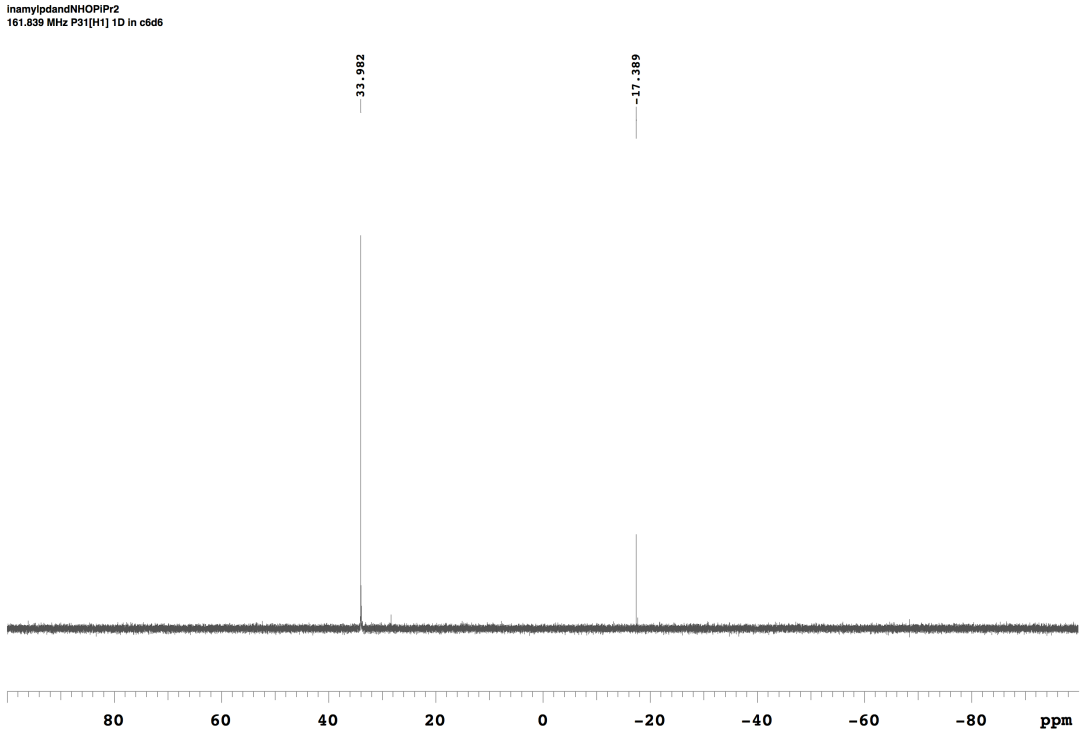

* impurity at -17.4 ppm is free ligand (IPr=CH)P^{i}Pr$_2$ (**2**)

Figure S19. ^{1}H NMR spectrum of (IPr=CH)^{i}Pr$_2$P•AuCl (**8**) in C_6D_6.

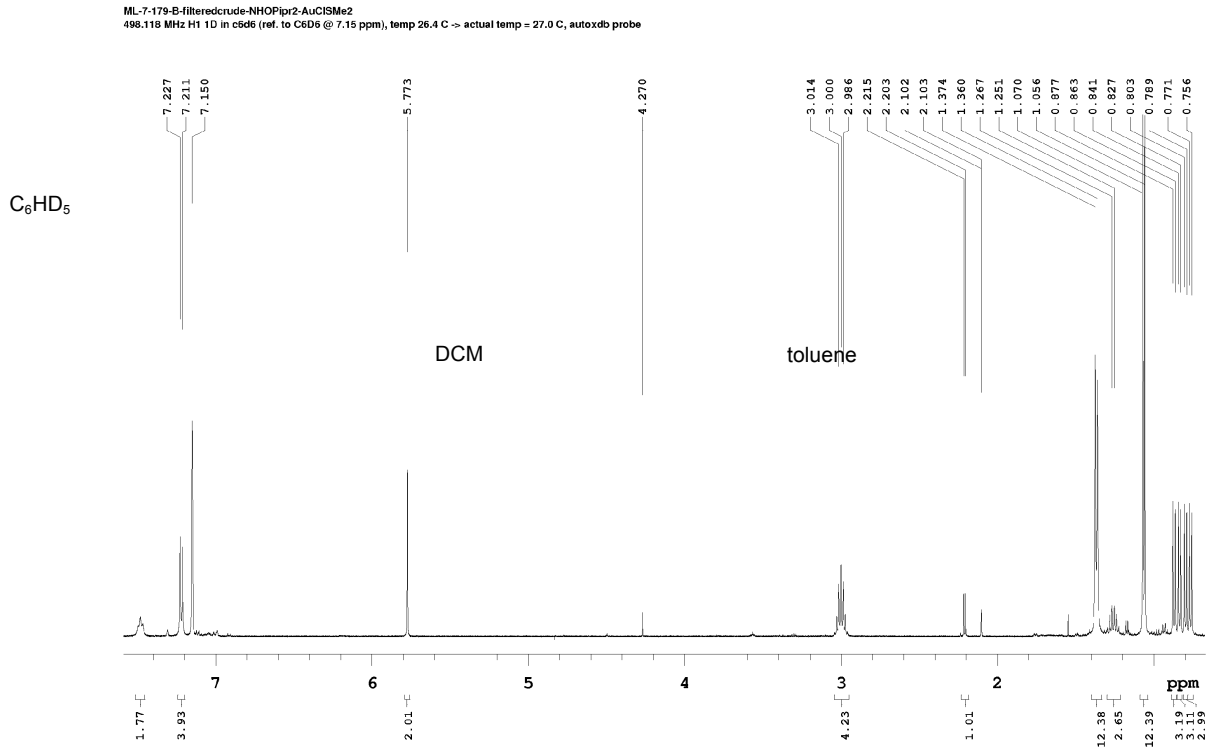

Figure S20. $^{13}C\{^{1}H\}$ NMR spectrum of (IPr=CH)^{i}Pr$_2$P•AuCl (**8**) in C_6D_6.

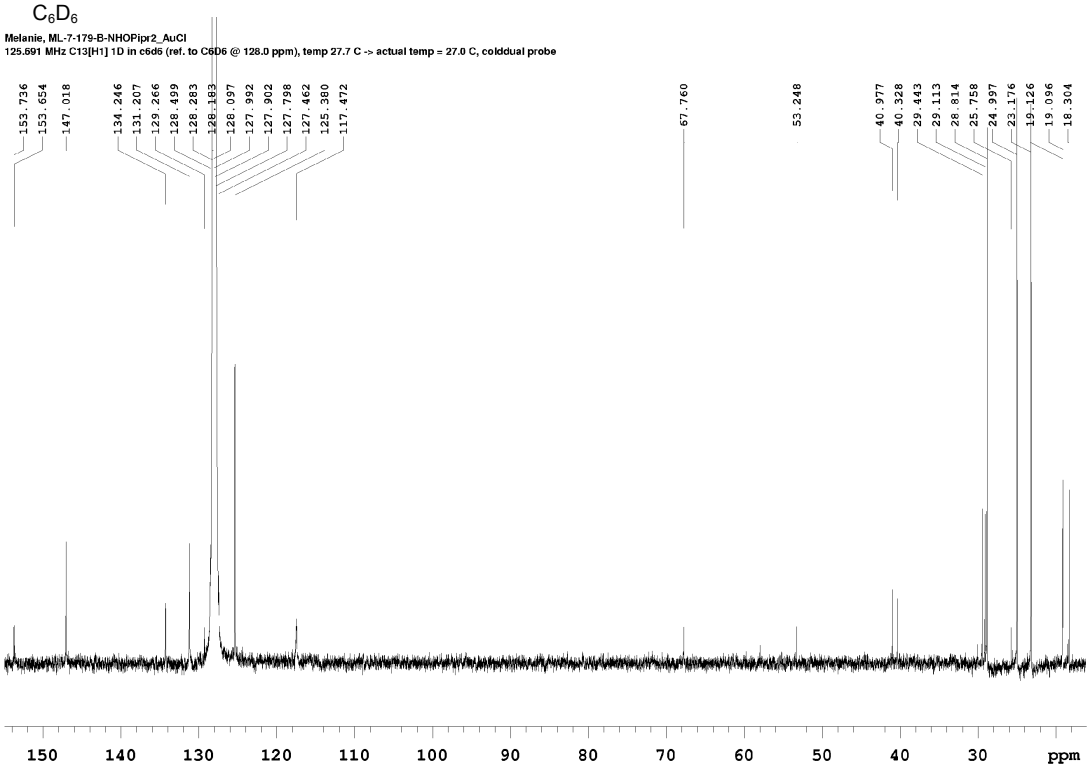

Figure S21. $^{31}P\{^{1}H\}$ NMR spectrum of (IPr=CH)^{i}Pr$_2$P•AuCl (**8**) in C_6D_6.

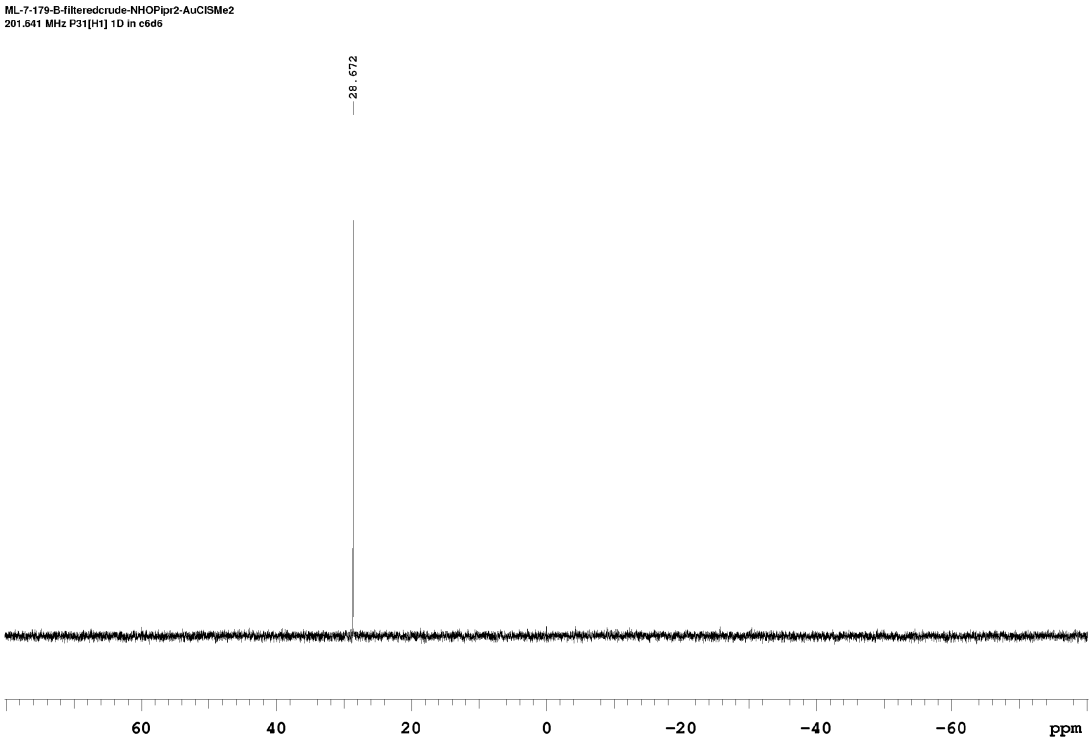

Figure S22. ^{1}H NMR spectrum of (IPr=CH)Ph_2P•AuCl (**9**) in C_6D_6.

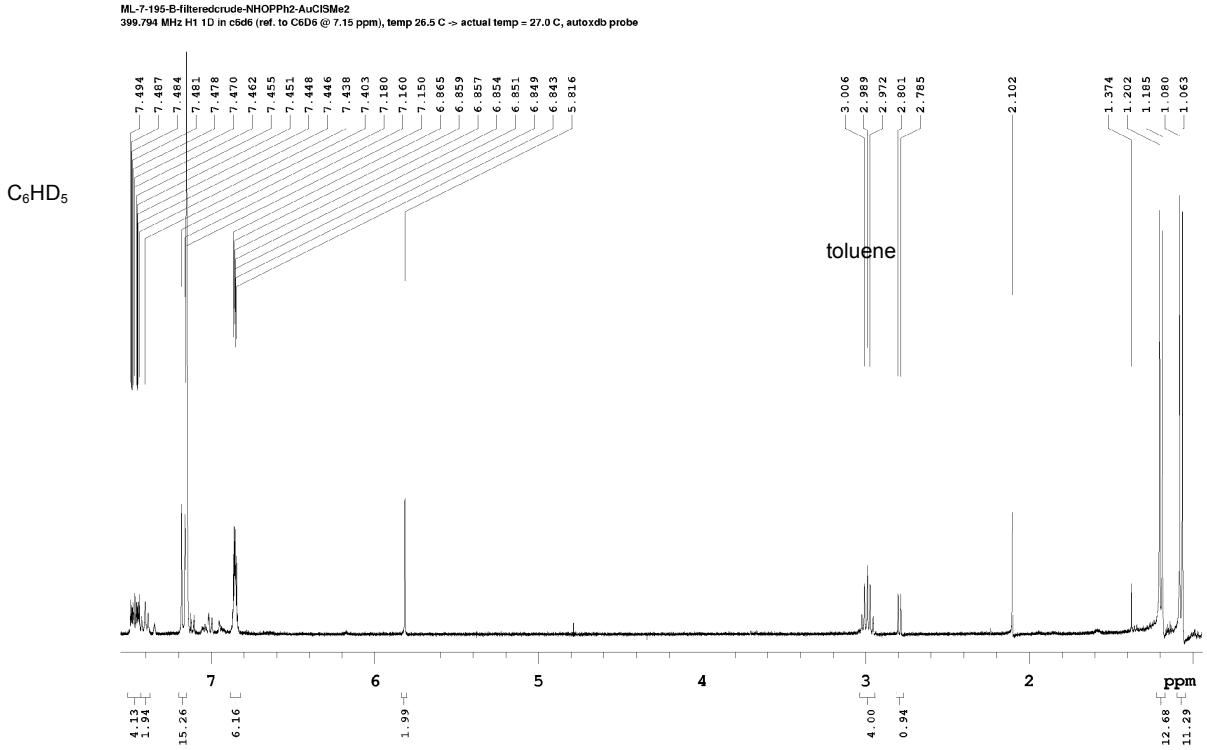

Figure S23. $^{13}C\{^{1}H\}$ NMR spectrum of (IPr=CH)Ph_2P•AuCl (**9**) in C_6D_6.

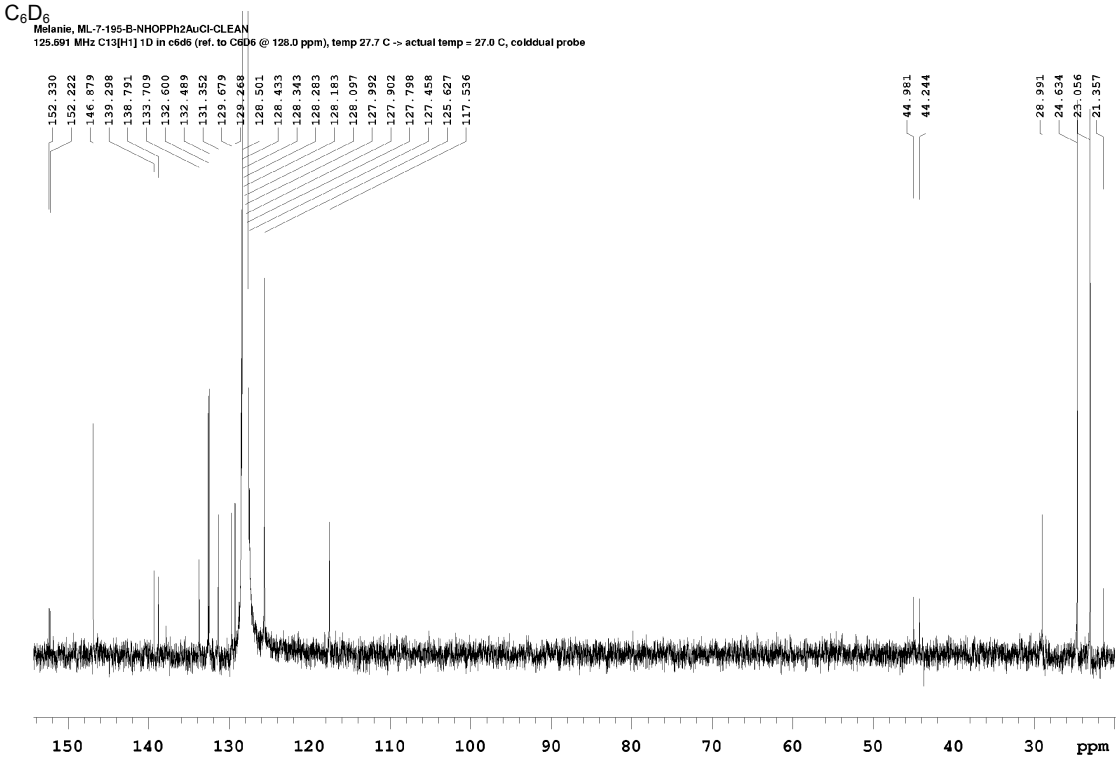

Figure S24. $^{31}P\{^{1}H\}$ NMR spectrum of (IPr=CH)Ph_2P•AuCl (**9**) in C_6D_6.

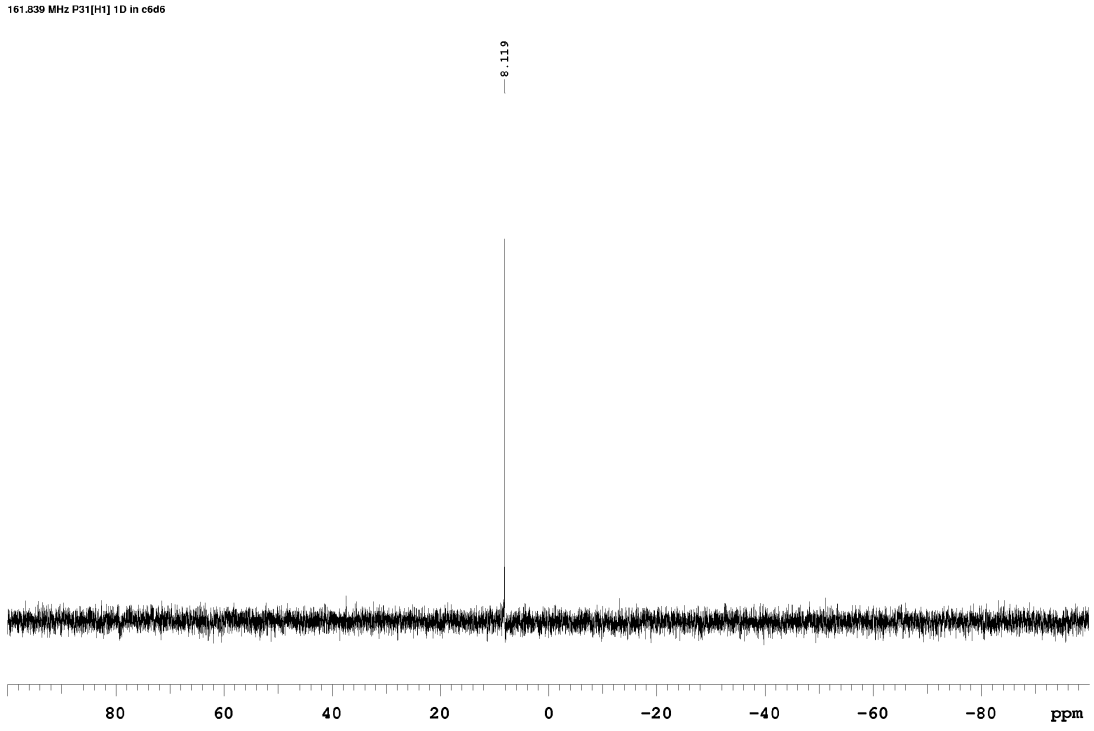

Figure S25. ^{1}H NMR spectrum of [IPr-CH_2-PPh_2•$AuAr^F$][$BAr^F{}_4$] (**10**) in $CDCl_3$.

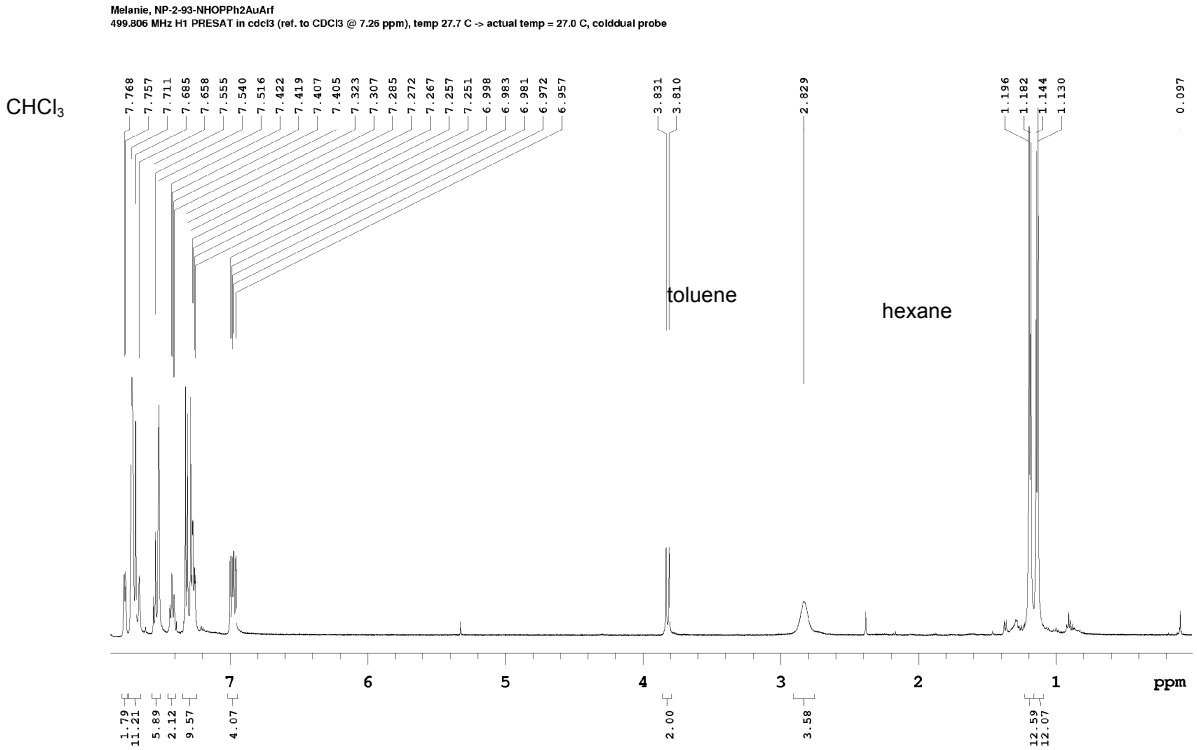

Figure S26. $^{11}B\{^{1}H\}$ NMR spectrum of [IPr-CH_2-PPh_2•$AuAr^F$][BAr^F_4] (**10**) in $CDCl_3$.

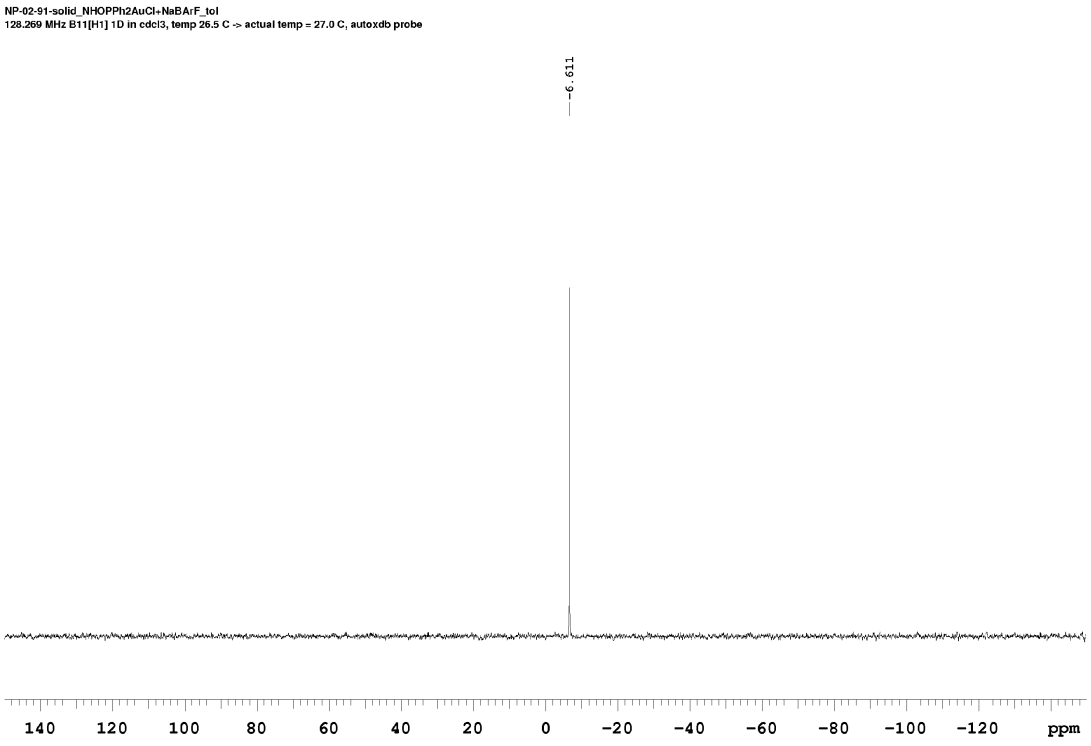

Figure S27. $^{13}C\{^{1}H\}$ NMR spectrum of [IPr-CH_2-PPh_2•$AuAr^F$][BAr^F_4] (**10**) in $CDCl_3$.

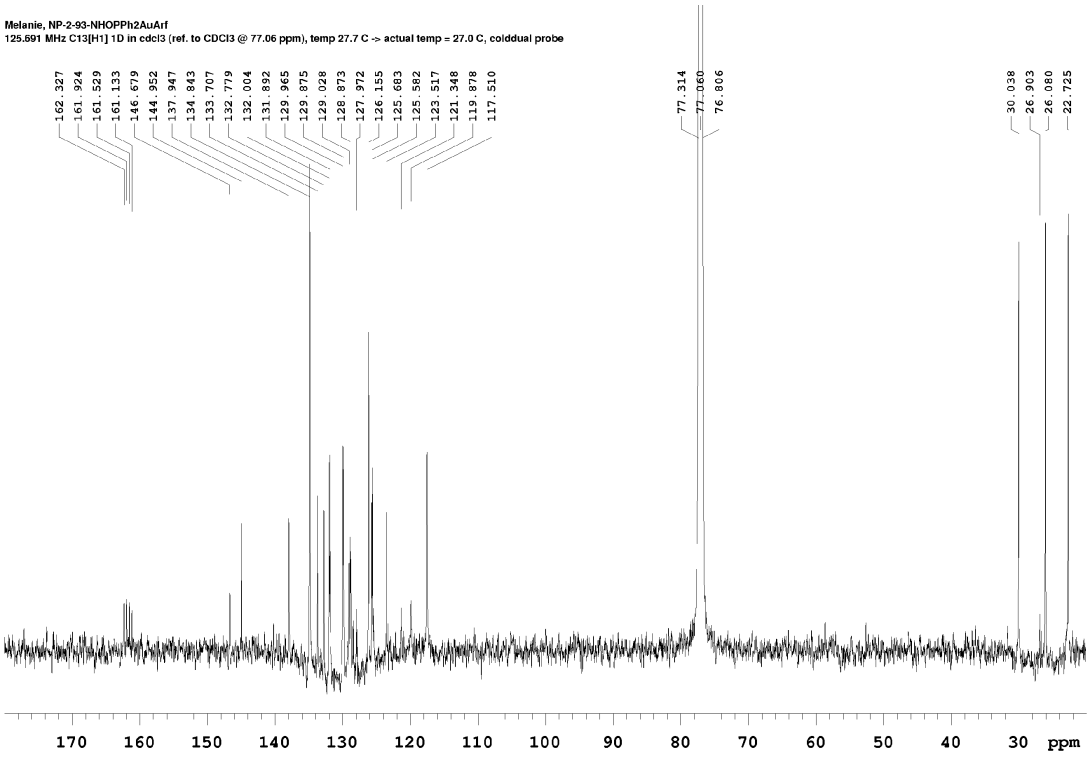

Figure S28. ^{19}F NMR spectrum of [IPr-CH_2-PPh_2•$AuAr^F$][$BAr^F{}_4$] (**10**) in $CDCl_3$.

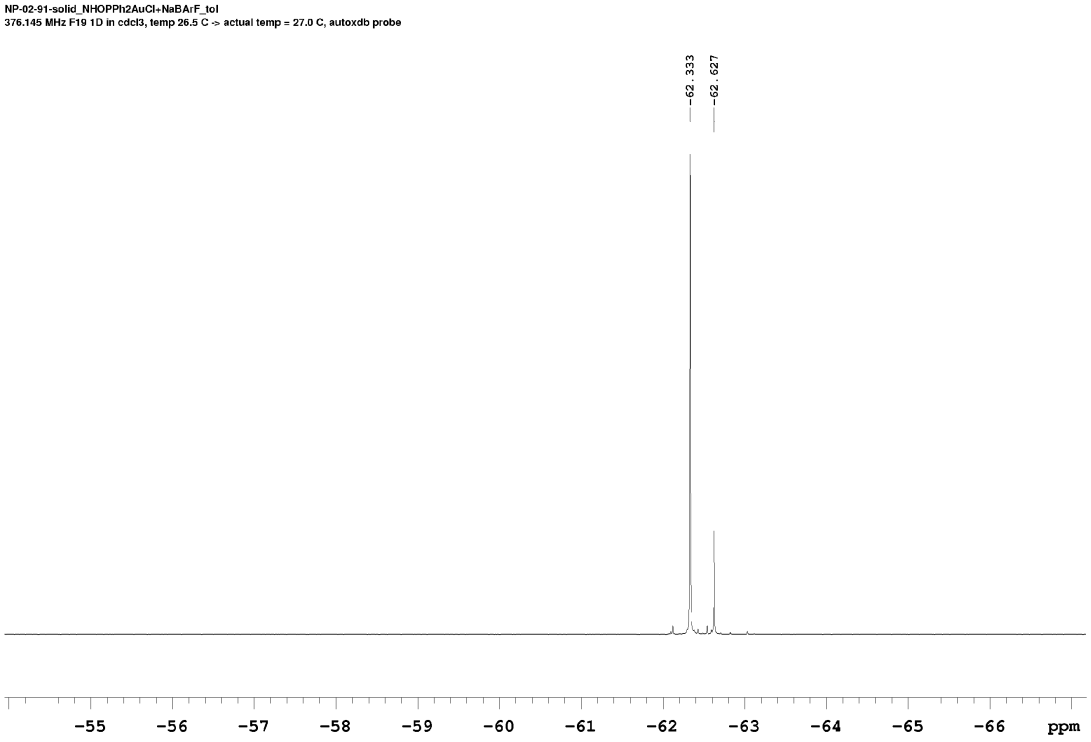

Figure S29. $^{31}P\{^{1}H\}$ NMR spectrum of [IPr-CH_2-PPh_2•$AuAr^F$][$BAr^F{}_4$] (**10**) in $CDCl_3$.

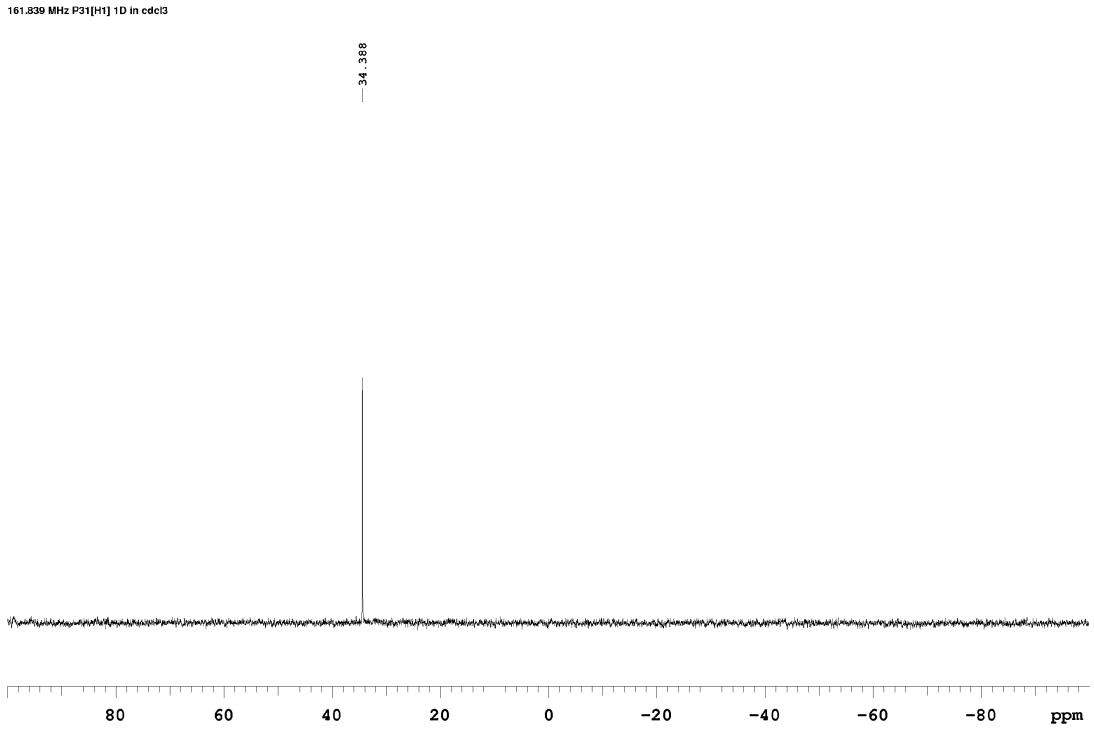

Figure S30. ^{1}H NMR spectrum of (IPr=CH)NMe$_2$•AuCl (**11**) in C_6D_6.

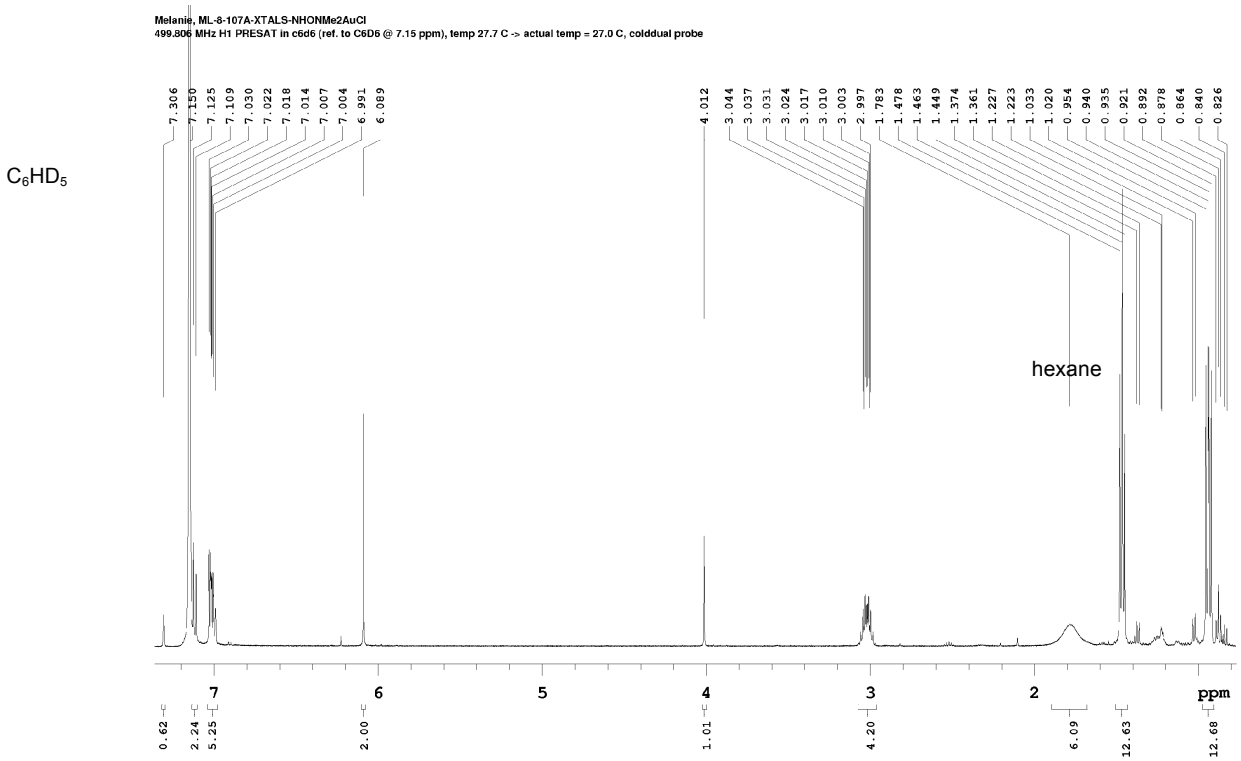

Figure S31. $^{13}C_6D_6\{1H\}$ NMR spectrum of (IPr=CH)NMe_2•AuCl (**11**) in C_6D_6.

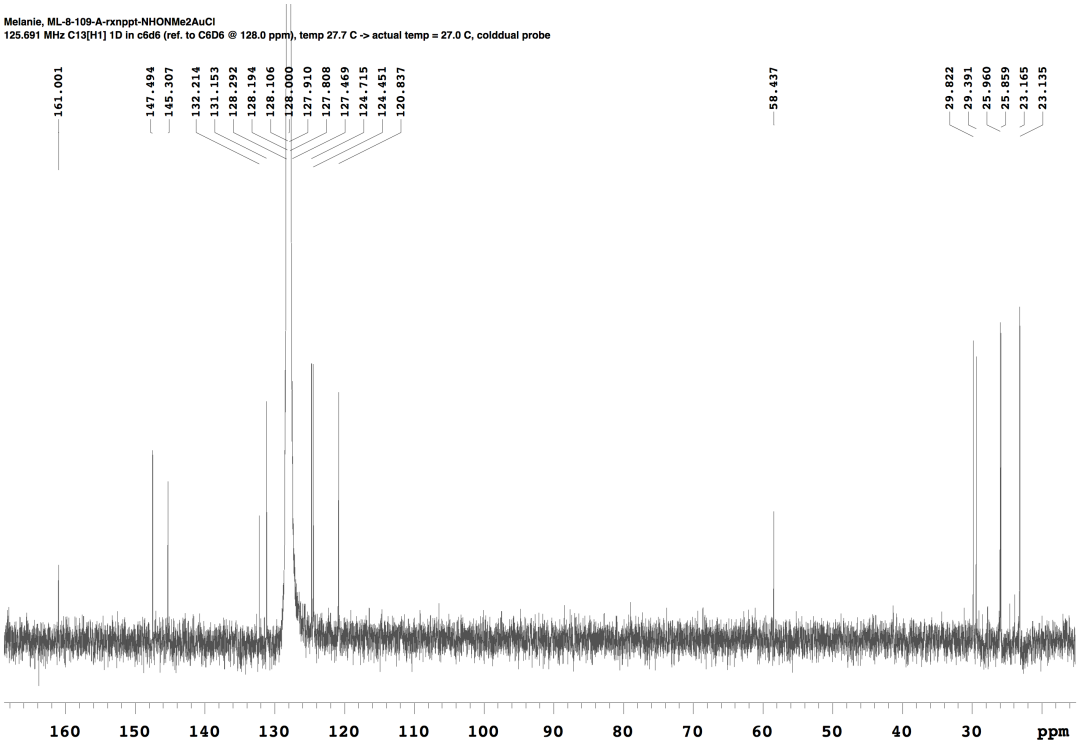

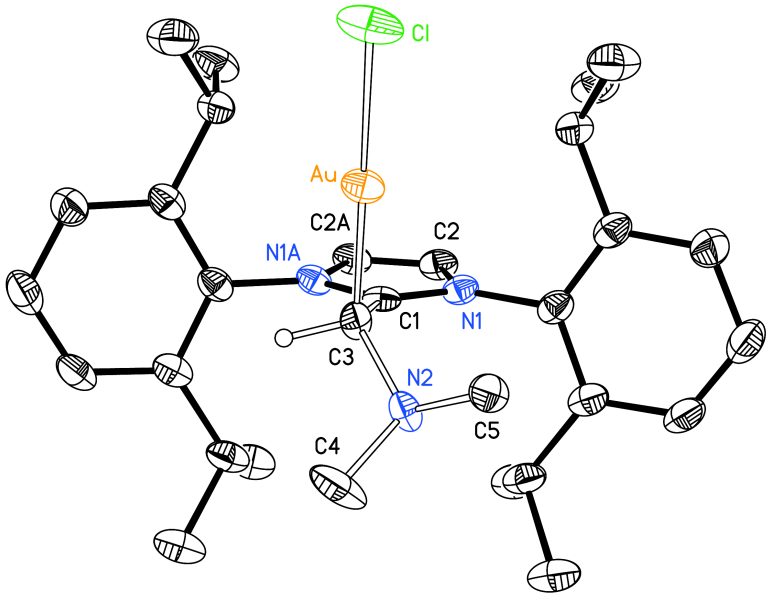

Figure S32. Molecular structure of (IPr=CH)NMe_2•AuCl (**11**) with thermal ellipsoids presented at a 30 % probability level. The hydrogen atom at C(3) is shown with an arbitrarily small thermal parameter; all remaining hydrogen atoms have been omitted for clarity. Selected bond lengths (Å) and angles (°): Au-C(3) 2.044(15), Au-Cl 2.300(4), C(3)-N(2) 1.44(2); Cl-Au-C(3) 177.6(4), C(1)-C(3)-Au 108.2(8), C(1)-C(3)-N(2) 110.9(16).

Table S1. Crystallographic Experimental Details for **11**.

A. Crystal Data	
formula	$C_{30}H_{43}AuClN_3$
formula weight	678.09
crystal dimensions (mm)	0.11 × 0.10 × 0.05
crystal system	monoclinic
space group	$P2_1/m$ (No. 11)
unit cell parameters[a]	
a (Å)	8.9505 (3)
b (Å)	18.1602 (7)
c (Å)	9.8838 (3)
β (deg)	110.4098 (17)
V (Å^3)	1505.69 (9)
Z	2
ρ_{calcd} (g cm^{-3})	1.496
μ (mm^{-1})	10.14
B. Data Collection and Refinement Conditions	
diffractometer	Bruker D8/APEX II CCD[b]
radiation (λ [Å])	Cu Kα (1.54178) (microfocus source)
temperature (°C)	–100
scan type	ω and ϕ scans (1.0°) (5 s exposures)
data collection 2θ limit (deg)	146.18
total data collected	10578 (-11 ≤ h ≤ 10, -22 ≤ k ≤ 22, -12 ≤ l ≤ 12)
independent reflections	3026 (R_{int} = 0.0306)
number of observed reflections (*NO*)	2927 [$F_o^2 \geq 2\sigma(F_o^2)$]
structure solution method	intrinsic phasing (*SHELXT-2014*[c])
refinement method	full-matrix least-squares on F^2 (*SHELXL–2014*[d])
absorption correction method	Gaussian integration (face-indexed)
range of transmission factors	0.7213–0.4106
data/restraints/parameters	3026 / 0 / 189
goodness-of-fit (S)[e] [all data]	1.359
final R indices[f]	
R_1 [$F_o^2 \geq 2\sigma(F_o^2)$]	0.0606
wR_2 [all data]	0.1230
largest difference peak and hole	2.060 and –4.228 e Å^{-3}

[a]Obtained from least-squares refinement of 9990 reflections with 9.54° < 2θ < 144.30°.

(continued)

Table S1. Crystallographic Experimental Details for **11** (continued)

[b]Programs for diffractometer operation, data collection, data reduction and absorption correction were those supplied by Bruker. The crystal used for data collection was the 'best' of a batch of low quality crystals. The unit cell was indexed using the program CELL_NOW, and the major component fit ~60% of the thresholded reflections. There were at least an additional six components, and attempts to integrate a multicomponent dataset were not particularly successful. The noisy difference map can most likely be attributed to the fact that there are a number of additional partially overlapping components contributing to the measured intensities (this is also apparent in the list of most disagreeable reflections in the SHELXL-2014 output with I_{obs} larger than I_{calc} for the top 50 reflections). Attempts to refine the structure in $P2_1$ instead to $P2_1/m$ gave massive correlations of the ADPs and a more poorly-behaved structure. New crystallization experiments are currently underway in the hope of yielding better quality single crystals.

[c]Sheldrick, G. M. *Acta Crystallogr.* **2015**, *A71*, 3–8. (*SHELXT-2014*)

[d]Sheldrick, G. M. *Acta Crystallogr.* **2015**, *C71*, 3–8. (*SHELXL-2014*)

[e]$S = [\Sigma w(F_o^2 - F_c^2)^2/(n - p)]^{1/2}$ (n = number of data; p = number of parameters varied; $w = [\sigma^2(F_o^2) + 11.7041P]^{-1}$ where $P = [\mathrm{Max}(F_o^2, 0) + 2F_c^2]/3$).

[f]$R_1 = \Sigma||F_o| - |F_c||/\Sigma|F_o|$; $wR_2 = [\Sigma w(F_o^2 - F_c^2)^2/\Sigma w(F_o^4)]^{1/2}$.